Supporting Information

CeO_2-Enhanced Surface Reconstruction of Ni_3S_2 Nanosheets for Improved Urea-Assisted Water Splitting Performance

Jiale Shang[a], Tong Wei[a], Xiaoqing Yan[b], Zheng Fang[a], Leilei Du[a], Jichao Shi[a], Fozia Sultana[a,*], Tongtong Li[a,*], Renhong Li[a,*]

[a.] National Engineering Lab for Textile Fiber Materials and Processing Technology, School of Materials Science & Engineering, Zhejiang Sci-Tech University, Hangzhou 310018, China.

[b.] Department of Chemistry, College of Science, Zhejiang Sci-Tech University, Hangzhou, 310018, PR China.

E-mail addresses: lirenhong@zstu.edu.cn (R. Li), yitaji@zstu.edu.cn (T. Li), foziasultana174@yahoo.com (Fozia Sultana)

Experimental section

1. Structural Characterisations

X-ray diffraction (XRD) analysis was performed on a Bruker D8 diffractometer using Cu Kα radiation (λ = 1.54056 Å). Scanning electron microscopy (SEM) and corresponding energy dispersive spectroscopy (EDS) images were acquired from ZEISS Sigma 300 microscope equipped with ZEISS Sigma 300 Essence™ EDS. Transmission electron microscopy (TEM) images of the catalysts were recorded by FEI Talos F200X instruments after exfoliating the composites from the NF matrix via ultrasonication treatment for 8 hours. X-ray photoelectron spectroscopy (XPS) analysis was carried out on a Thermo Scientific K-Alpha, with all binding energies calibrated by referencing to C1s peak at 284.8 eV. Raman investigations were gathered from a laser confocal Raman microspectrometer (Horiba LabRAM HR Evolution) with a wavelength of 532 nm as the excitation source. Electron paramagnetic resonance (EPR) spectra were recorded using a Bruker EMXplus-6/1.

2. Electrochemical measurements

The electrochemical tests were performed in a classical three-electrode configuration using an Interface 5000E electrochemical workstation. The graphite rod electrode served as counter electrode and the Hg/HgO electrode (filled with 1.0 M KOH) were used as reference electrode, respectively. The as-prepared Ni_3S_2-CeO_2/NF catalyst was sectioned into 1.0 cm × 1.0 cm pieces for use as the working electrode. Cyclic voltammetry (CV) was conducted over the potential range of 0 to 1.0 Vs. RHE for UOR/OER and from −1.0 to −1.5 Vs. RHE for HER at a scan rate of 50 mV s^{-1} to activate the catalysts and obtain stable CV curves. To evaluate the performance of the urea oxidation reaction (UOR), polarization curves were obtained using linear sweep voltammetry at a scan rate of 2 mV/s in a 1 M KOH solution containing 0.50 M urea. The Tafel slope was determined by fitting the linear region of the linear sweep voltammetry (LSV) curves using the Tafel equation, expressed as: $\eta = a + b \log |j|$, where η denotes the overpotential, j represents the current density, and a and b are constants, with b specifically representing the Tafel slope. Electrochemical impedance

spectroscopy (EIS) was performed by applying an AC amplitude of 5 mV s^{-1} over a frequency range from 10^5 to 10^{-1} Hz. The double-layer capacitances (C_{dl}) of synthesized samples were derived from their cyclic voltammetry (CV) plots recorded at scan rates of 20, 40, 60, 80, and 100 mV/s within a potential window of −0.15 to −0.05 V vs. RHE, in the non-Faradaic region. The electrochemical surface area (ECSA) was evaluated using the equation: ECSA = C_{dl}/Cs, where Cs represents the specific capacitance of a flat, smooth electrode surface under identical electrolyte conditions, with a value is 0.04 mF cm^{-2}. All potentials were corrected for 90 % iR compensation. The potentials reported in this study for the UOR, OER, and HER were referenced to the reversible hydrogen electrode (RHE) according to the equation: $E_{RHE} = E_{Hg/HgO}$+ 0.059 × pH + 0.098 V. In a two- electrode setup, the prepared electrodes were directly used as cathode and anode, and the polarization curves were obtained using linear sweep voltammetry from 1.0 to 2.0 V at a scan rate of 2 mV s^{-1} both in 1.0 M KOH or 1.0 M KOH with 0.50 M urea.

3. Calculation of Faradaic efficiency (FE%)

The H-type electrochemical cell coupled with a gas chromatograph (GC), was used to monitor the H_2 yield. The GC analysis utilized a 5977B mass spectrometer detector (Agilent Technologies) equipped with a thermal conductivity detector, using argon as the carrier gas with a purity of 99.999%. A constant cell voltage was maintained across the electrode and the H_2 production was analyzed at 8 minutes intervals. The Faradaic efficiency (FE) for H_2 production can be calculated by the following equation:

$$\text{FE } (H_2, \%) = \frac{N \times n \times F}{Q} \times 100\%$$

where n represents the numbers of transferred electrons (n = 2 for HER), F is the Faraday constant (96485 C mol^{-1}), N is the mole of generated H_2 obtained by gas chromatograph, Q is the charge passed through the electrode (C) gained from i-t test.

4. Operando surface-enhanced Fourier-transform infrared spectroscopy (SR-FTIR) analysis

Operando SR-FTIR experiments were conducted using a Bruker VERTEX

80/80V instrument, equipped with an Infrared spectral cell (EC-RAIR-II) from Spirit Road Instruments. The Infrared spectral cell is a reflective infrared device that utilizes calcium fluoride crystals as infrared transmission windows, with a cut-off energy of approximately 625 cm^{-1}. Prior to each experiment, the catalyst was immobilized on the surface of calcium fluoride crystals using a conductive metal film, which served as the working electrode. An Ag/AgCl electrode was utilized as the reference electrode, while a Pt wire served as the counter electrode. Subsequently, 30 mL of a 1M KOH solution containing 0.50 M urea was introduced into the electrolytic cell. Spectral signals were recorded within the wave number range of 600 to 4000 cm^{-1} using the chronopotential testing method, covering the range from the open-circuit potential (OCP) to 0.90 V vs. Ag/AgCl. Each measurement was preceded by maintaining a specific potential for 50 seconds. Furthermore, each IR absorption spectrum was obtained by averaging 32 scans, achieving a resolution of 4 cm^{-1}. Background spectra of the catalyst electrodes were gathered at the open circuit voltage and subsequently subtracted prior to each systematic measurement, ensuring accurate data collection in the context of the applied potential.

5. Computational Details

All calculations were conducted within the framework of density functional theory using the projector augmented wave method, as implemented in the Vienna Ab-initio Simulation Package (VASP).[1] The generalized gradient approximation proposed by Perdew, Burke, and Ernzerhof[2] was employed for the exchange-correlation potential, along with screened hybrid density functionals.[3] Van der Waals interactions were accounted for using the DFT-D3 approach.[4] The plane wave cutoff energy was set at 350 eV, and an energy convergence criterion of 10^{-5} eV was established for the iterative solution of the Kohn-Sham equations. A vacuum layer of 20 Å was introduced perpendicular to the sheet to avoid artificial interaction between periodic images. Brillouin zone integration was performed using a 2 × 2 × 1 K-mesh. All the structures were relaxed until the residual forces on the atoms fell below 0.02 eV/Å. The Gibbs free energy of hydrogen adsorption was determined to be consistent with our previous calculation method.[5]

The adsorption energy (E_{ads}) of urea and possible reaction intermediates on catalyst were calculated using the following formula:

$$E_{ads} = {}^{E_{urea/M}} - E_{M} - {}^{E_{urea}} \quad (1),$$

where ${}^{E_{urea/M}}$, E_{M}, and ${}^{E_{urea}}$ represented the total energy of adsorbed molecule and catalyst, the energy of catalyst, and the energy of adsorbates, respectively. According to this formula, a negative value for the adsorption energy represents a more stable adsorption process.

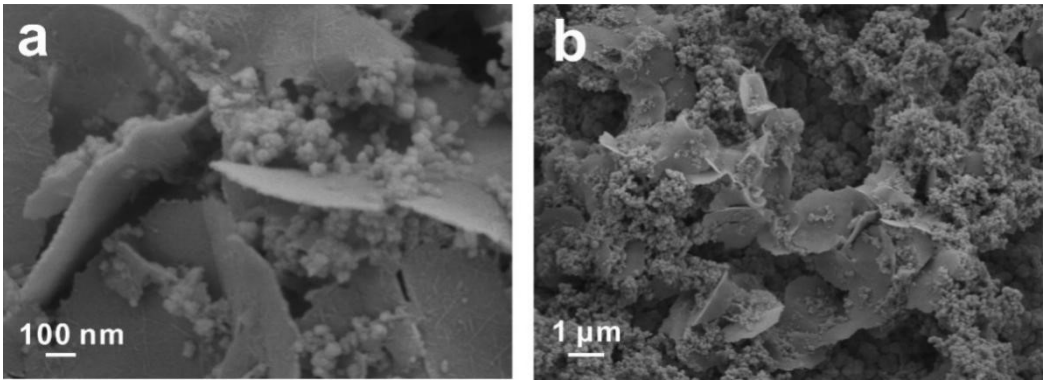

Fig. S1. High and low magnification SEM images of $Ni(OH)_2$-CeO_2/NF.

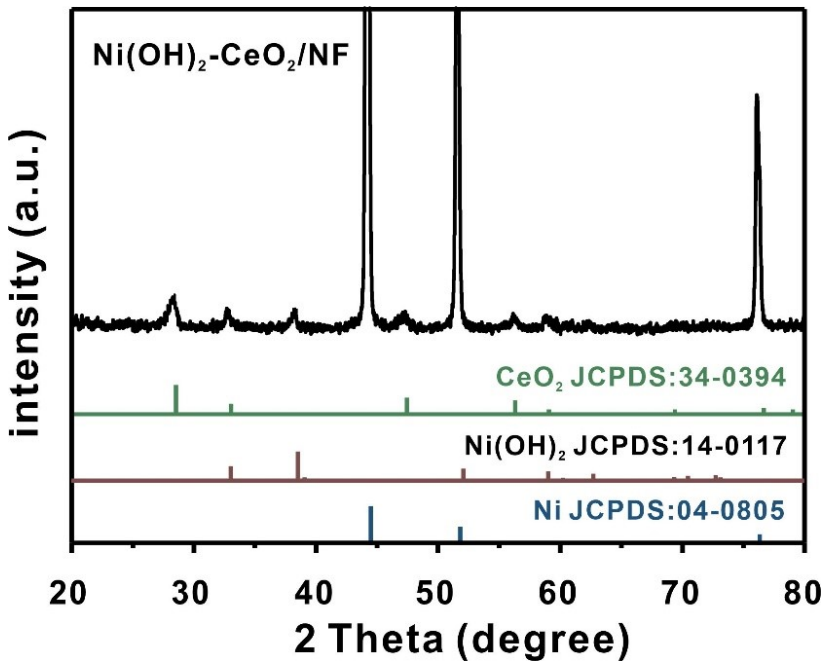

Fig S2. XRD pattern of $Ni(OH)_2$-CeO_2/NF.

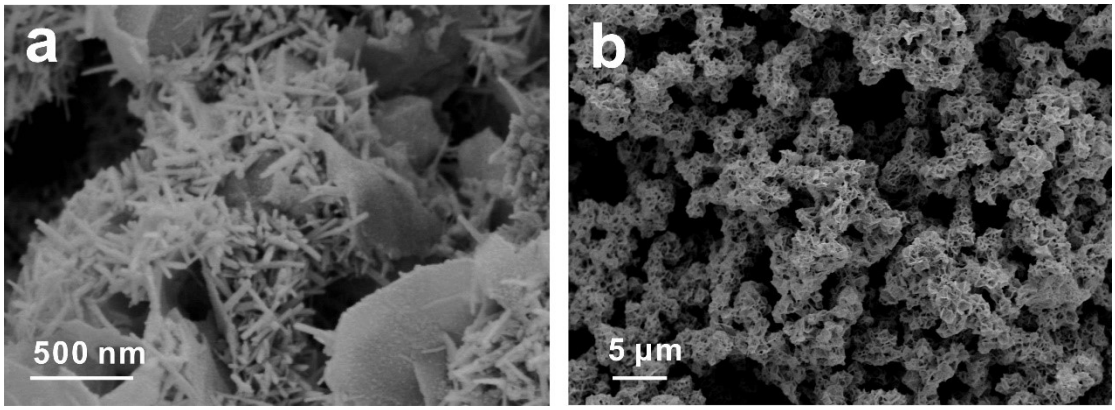

Fig. S3. High and low-magnification SEM images of Ni_3S_2-CeO_2/NF.

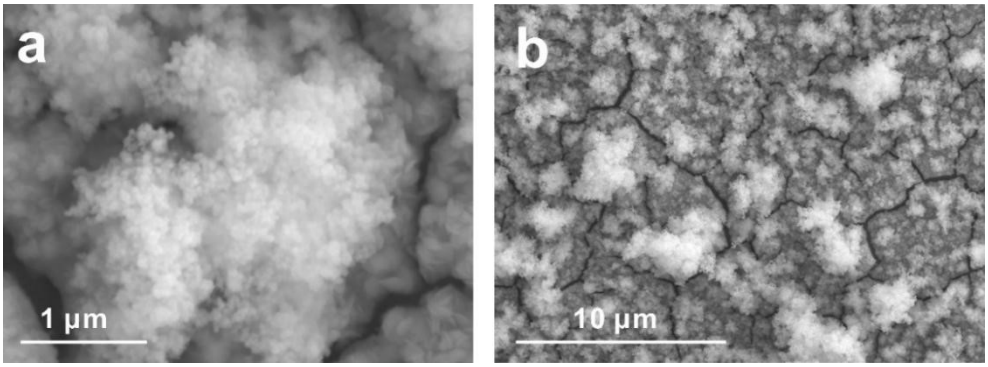

Fig. S4. High and low-magnification SEM images of CeO_2/NF.

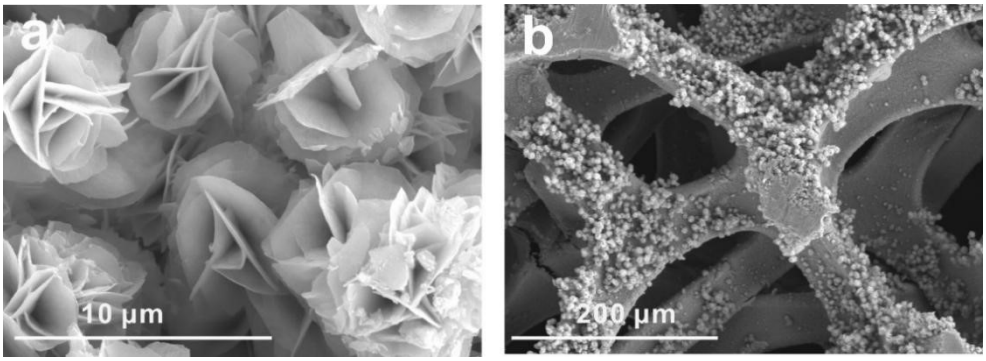

Fig. S5. High and low-magnification SEM images of Ni_3S_2/NF.

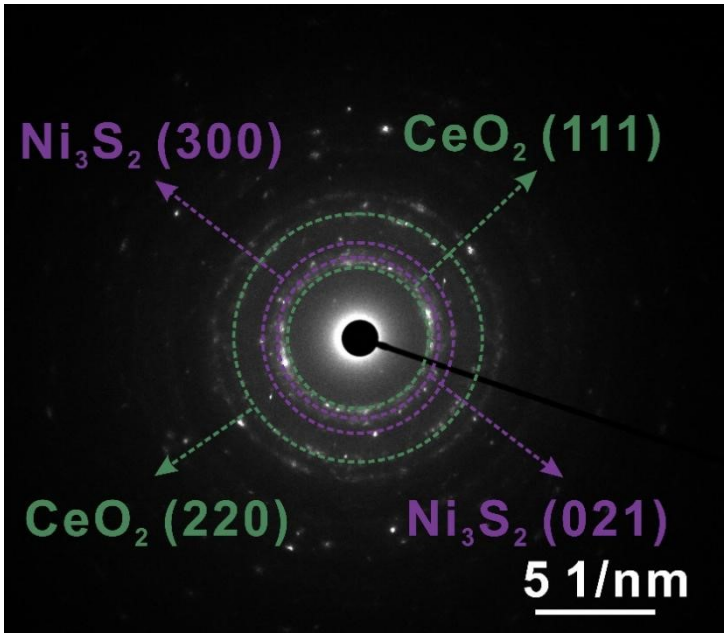

Fig. S6. SAED pattern of Ni_3S_2-CeO_2/NF.

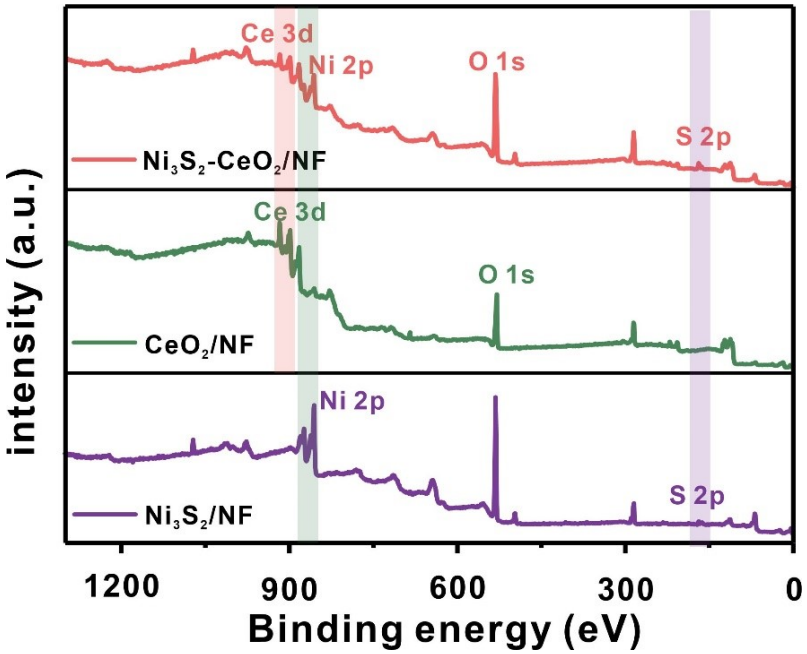

Fig. S7. XPS core-level spectra of Ni_3S_2-CeO_2/NF, CeO_2/NF and Ni_3S_2/NF.

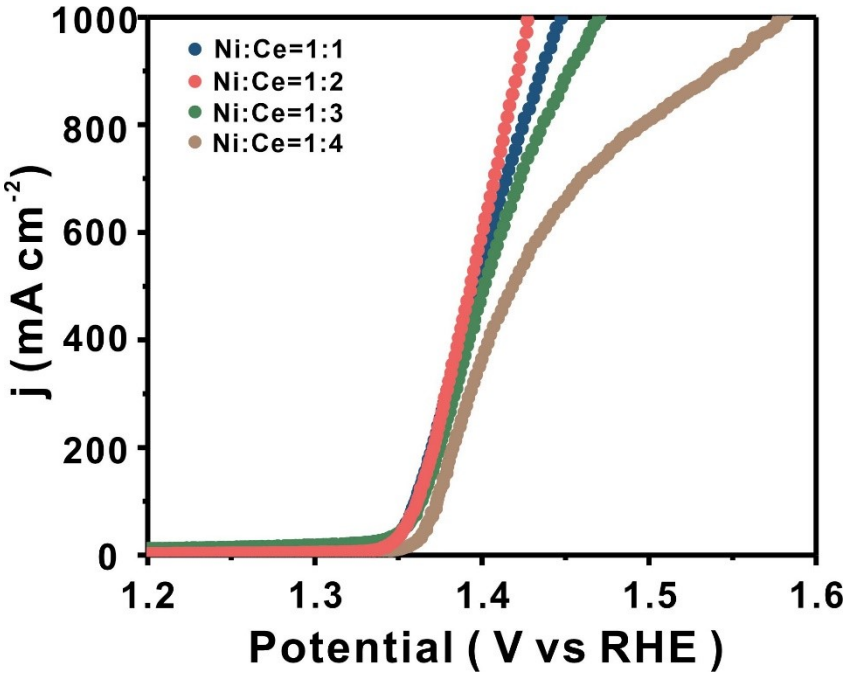

Fig. S8. UOR LSV curves of Ni_3S_2-CeO_2/NF catalysts for various Ni:Ce molar ratio.

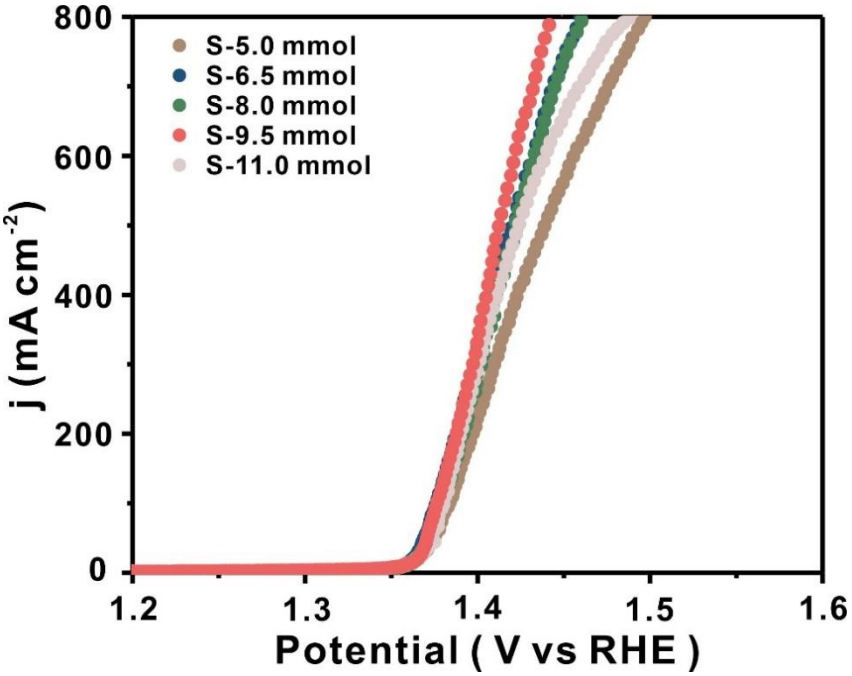

Fig. S9. UOR LSV curves of Ni_3S_2-CeO_2/NF catalyst with varying S content.

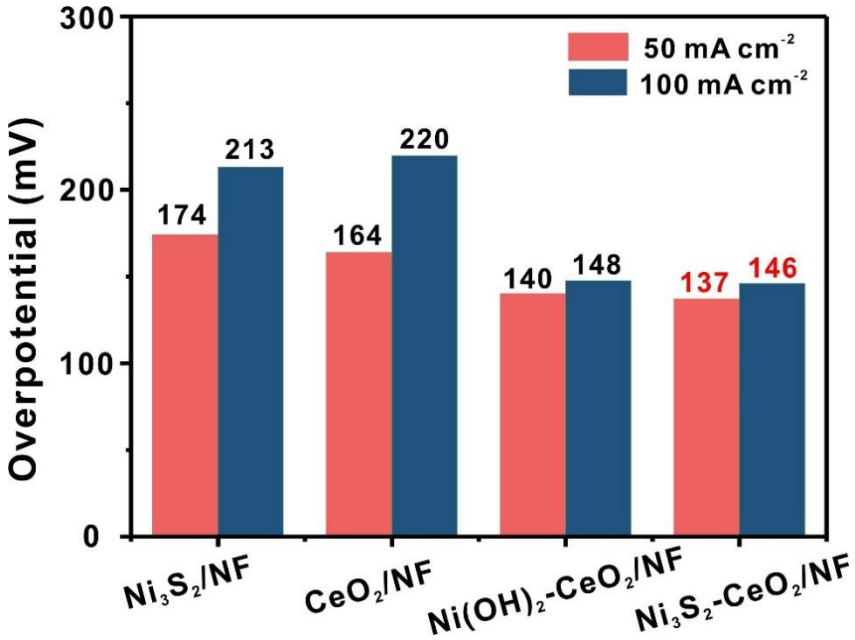

Fig. S10. Comparison of UOR overpotentials of Ni_3S_2-CeO_2/NF and its counterparts at current densities of 50 and 100 mA cm^{-2}.

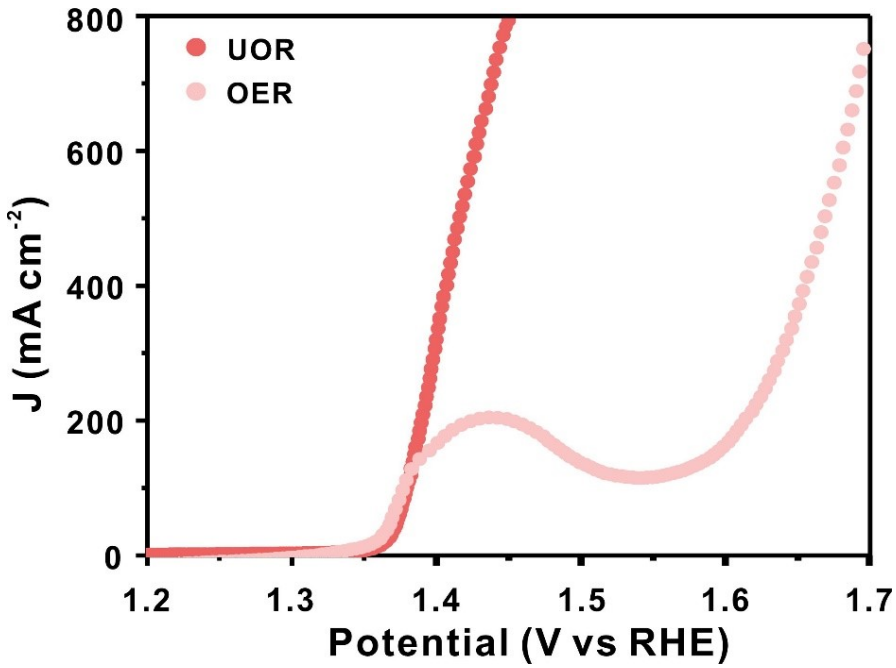

Fig. S11. LSV curves (with iR compensation) of Ni_3S_2-CeO_2/NF in 1.0 M KOH with and without 0.50 M urea.

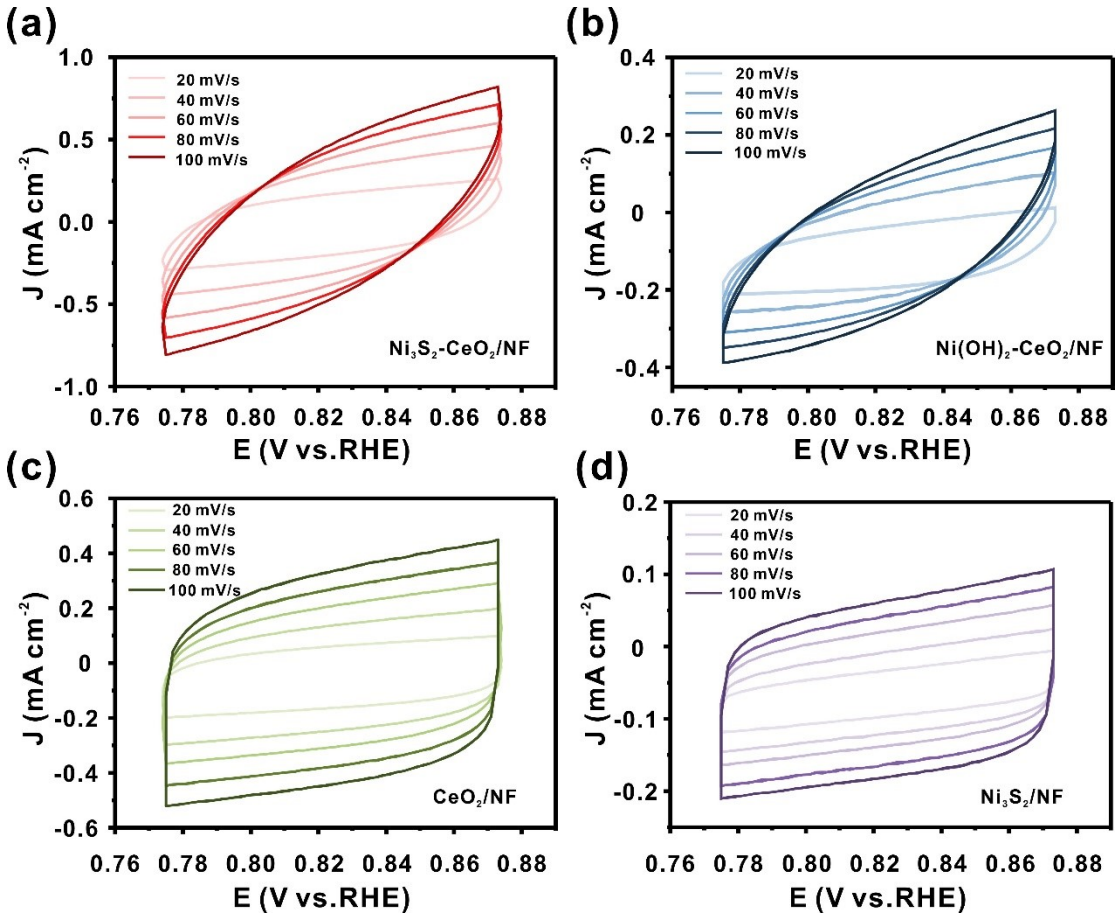

Fig. S12. Comparison of CV curves at various scan rates (20–100 mV s^{-1}) for (a) Ni_3S_2-CeO_2/NF, (b) $Ni(OH)_2$-CeO_2/NF, (c) CeO_2/NF and (d) Ni_3S_2/NF.

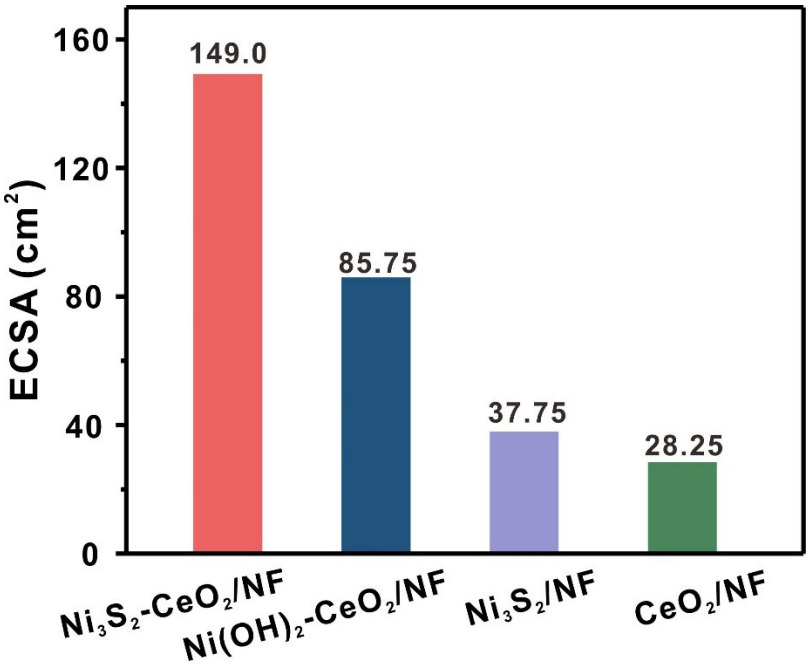

Fig. S13. Comparison of ECSAs of Ni_3S_2-CeO_2/NF and its various counterparts for UOR.

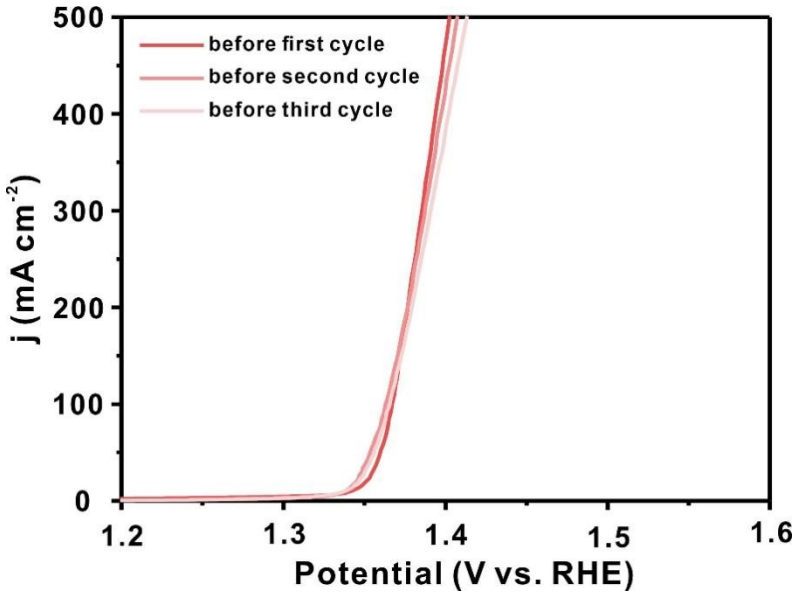

Fig. S14. Comparison of LSV curves of Ni_3S_2-CeO_2/NF before urea solution replacement during UOR stability test conducted every 16 hours.

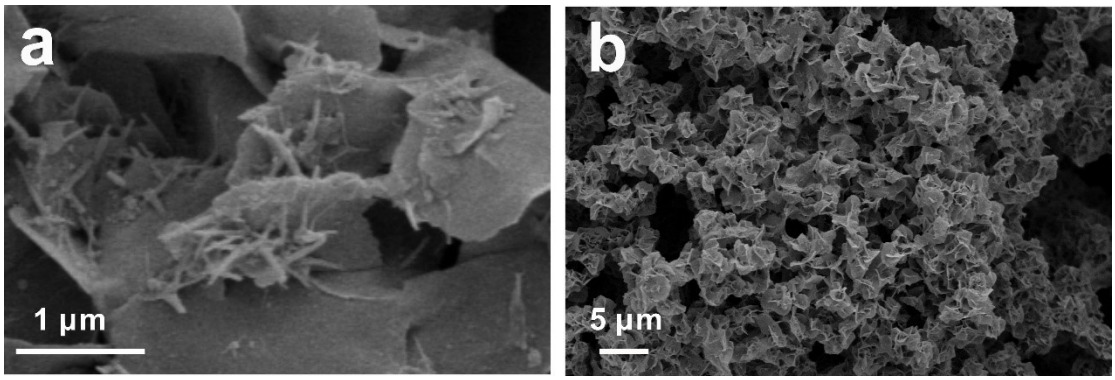

Fig. S15. SEM images of Ni_3S_2-CeO_2/NF following long-term durability test for UOR.

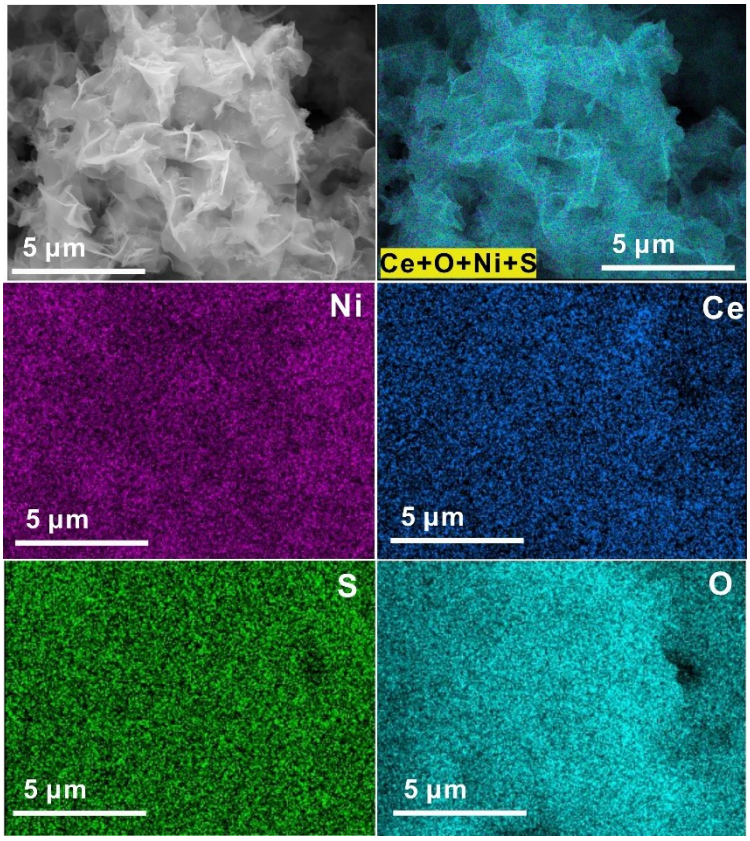

Fig. S16. EDS elemental mapping images of Ni_3S_2-CeO_2/NF after UOR.

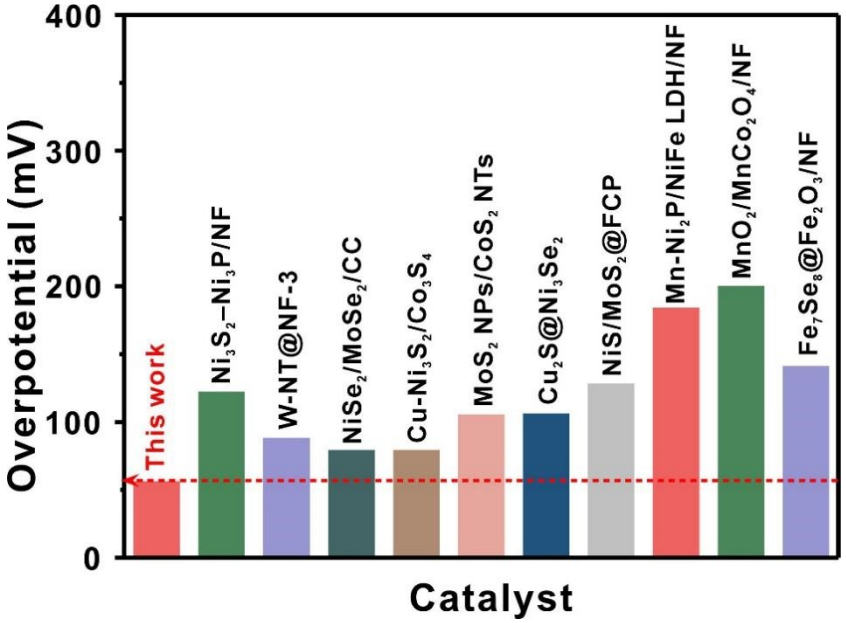

Fig. S17. Comparison of HER overpotentials (mV) at 10 mA cm^{-2} for Ni_3S_2-CeO_2/NF and recently reported electrocatalysts.

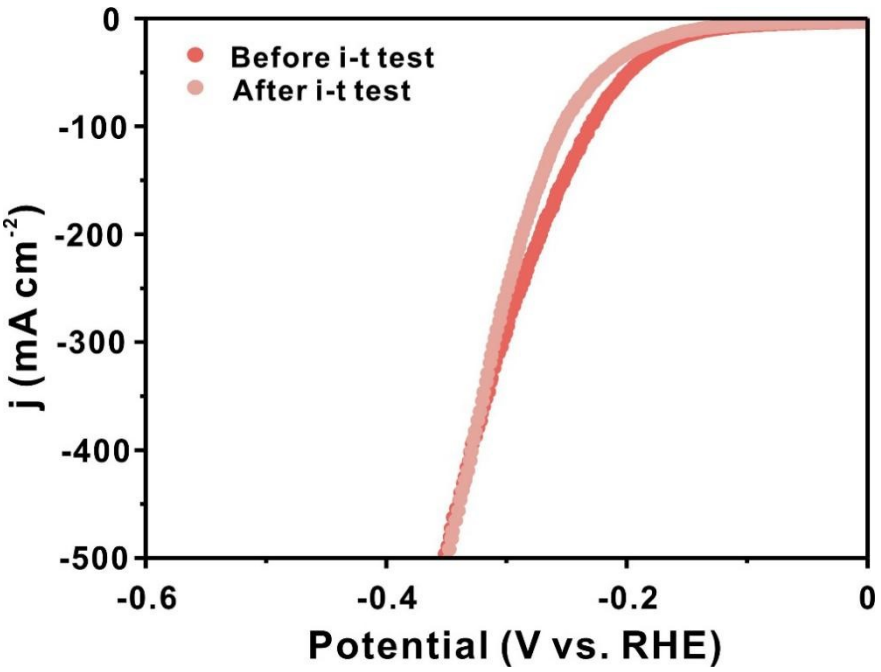

Fig. S18. LSV curves of Ni_3S_2-CeO_2/NF before and after 30 hours HER stability test.

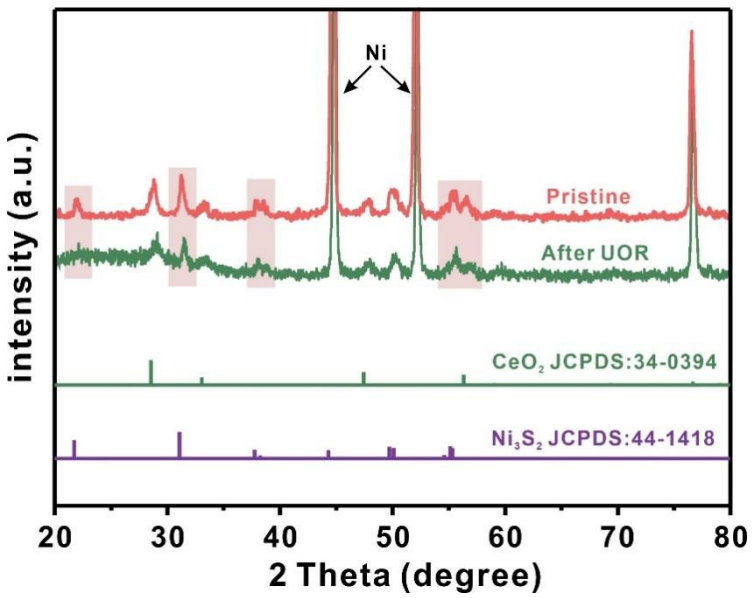

Fig. S19. Comparison of Ni_3S_2-CeO_2/NF XRD patterns before and after 10 hours UOR durability test.

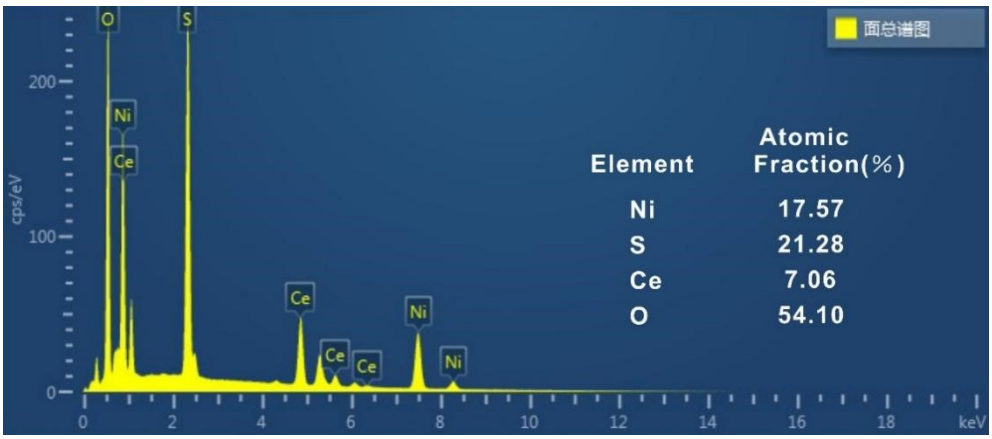

Fig. S20. EDX spectrum of Ni_3S_2-CeO_2/NF catalyst.

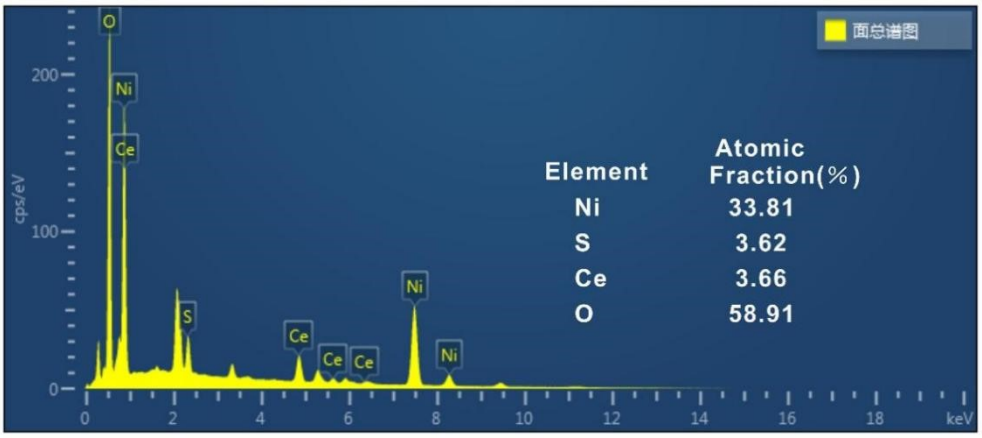

Fig. S21. EDX spectrum of Ni_3S_2-CeO_2/NF catalyst after UOR electrolysis.

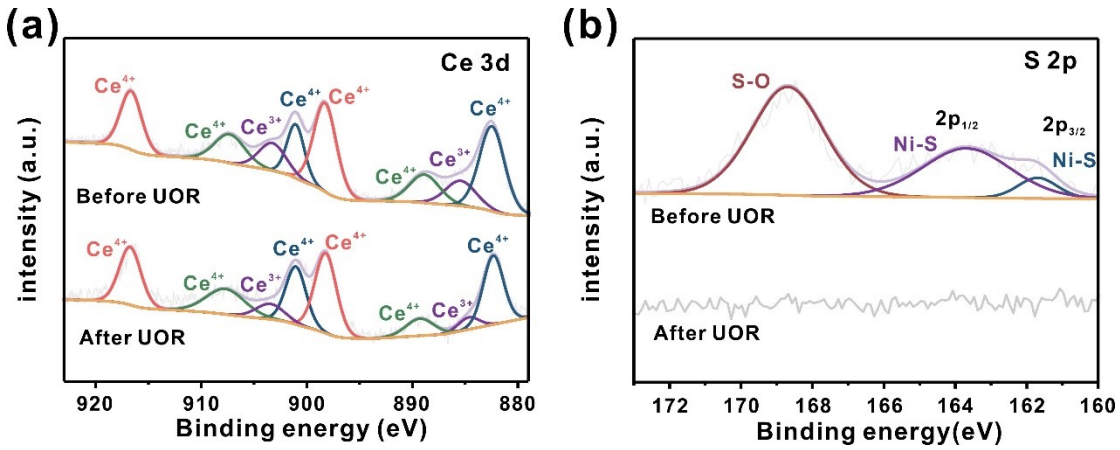

Fig. S22. XPS spectra of Ni_3S_2-CeO_2/NF: (a) Ce 3d and (b) S 2p before and after long-term UOR test.

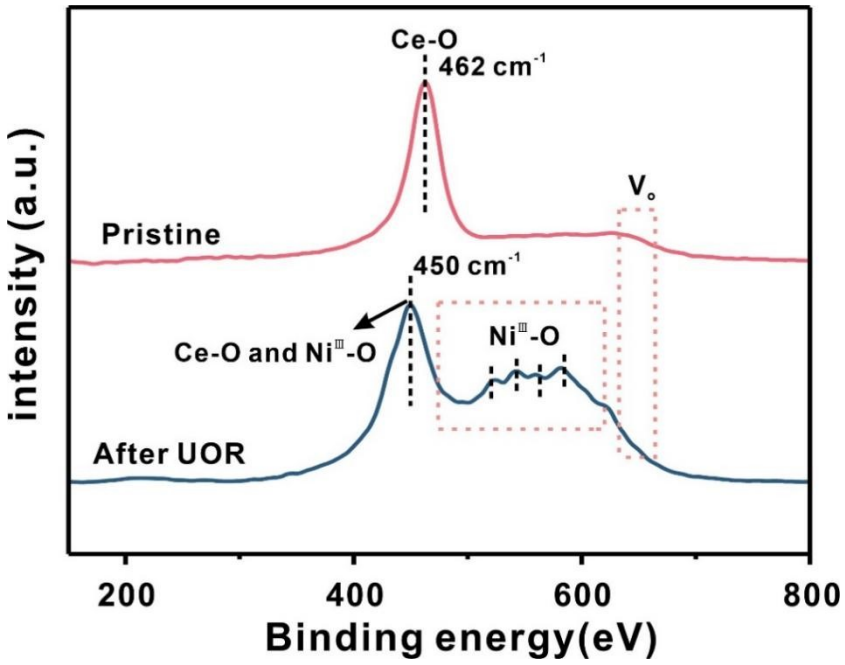

Fig. S23. Raman spectra of Ni_3S_2-CeO_2/NF before and after UOR test.

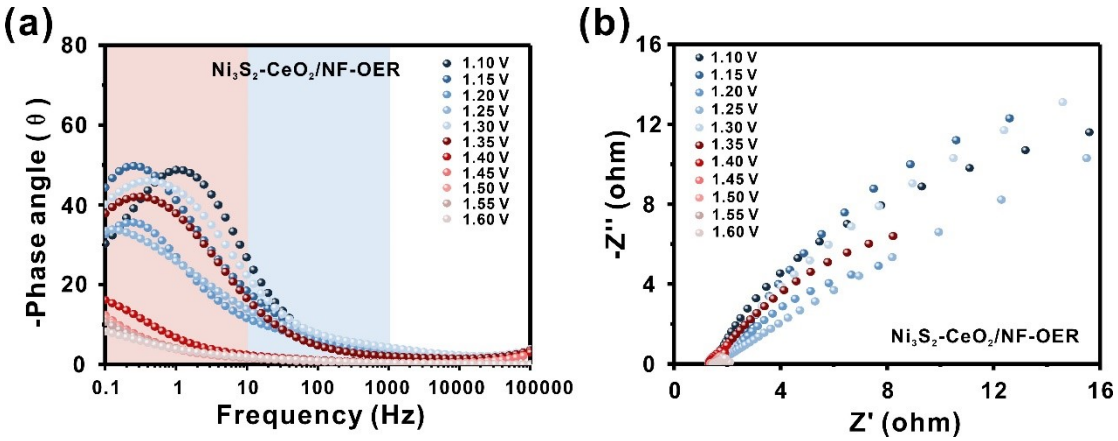

Fig. S24. Mechanistic study of Ni_3S_2-CeO_2/NF during UOR at various potentials in 1.0 M KOH: (a) Bode plots and (b) Operando Nyquist plots.

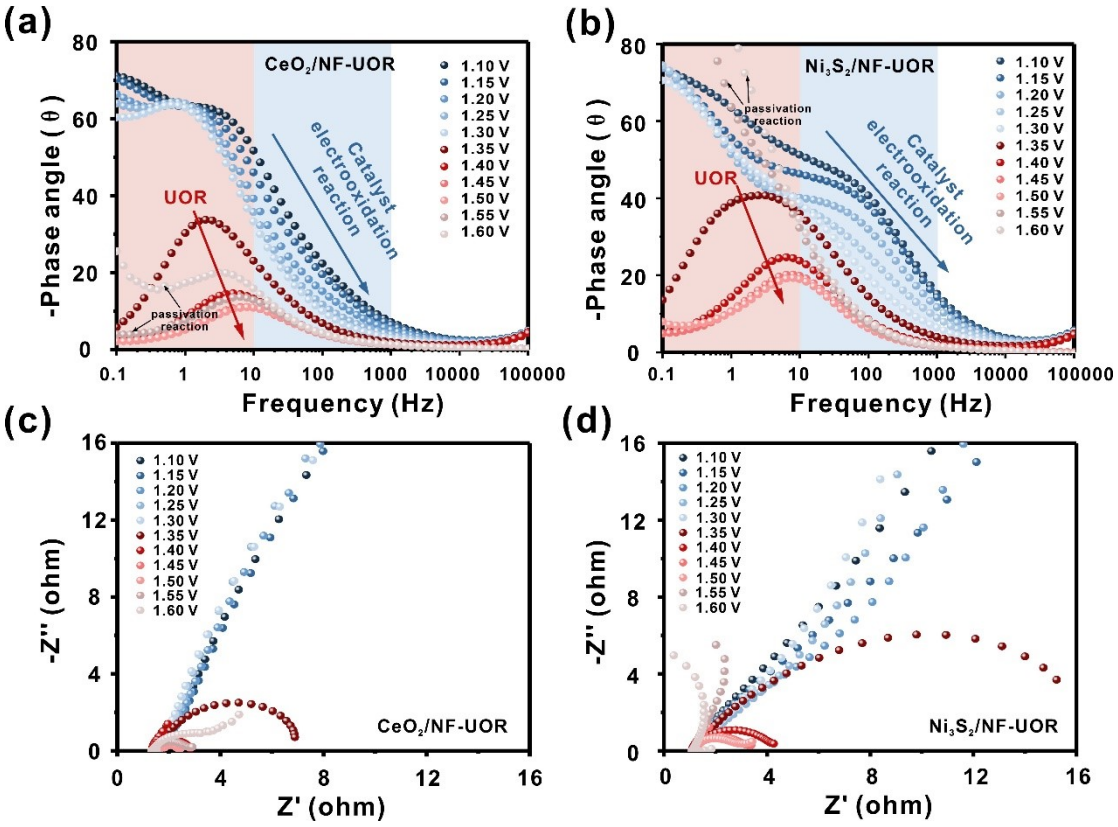

Fig. S25. Bode plots at various potentials in 1.0 M KOH with 0.50 M urea of: (a) CeO_2/NF and (b) Ni_3S_2 /NF, Operando Nyquist plots at various potentials in 1.0 M KOH with 0.50 M urea: (c) of CeO_2/NF and (d) Ni_3S_2 /NF.

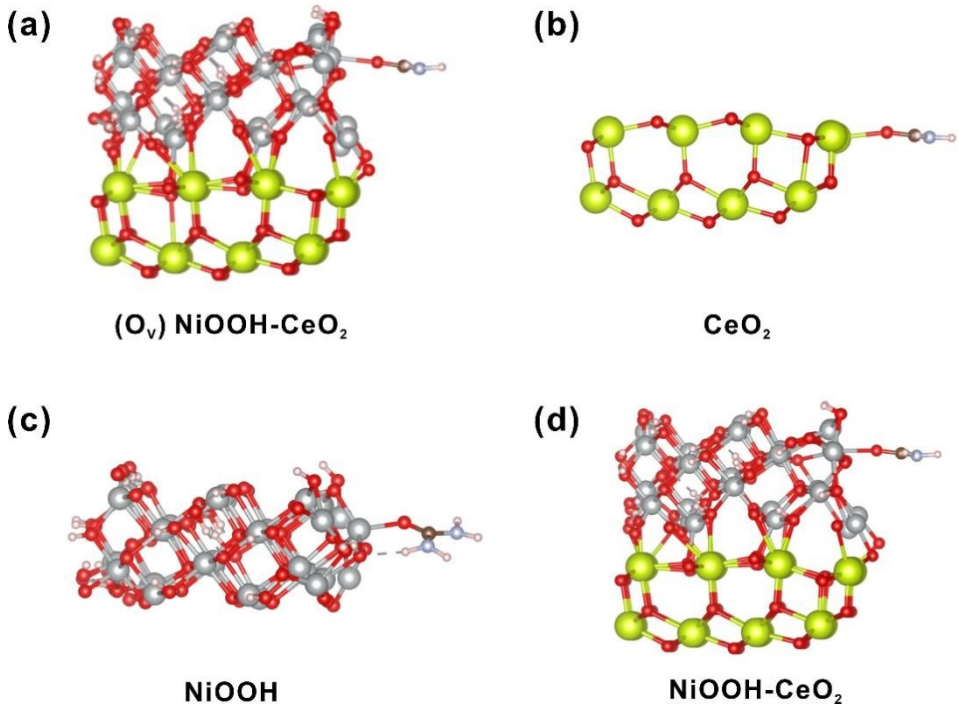

Fig. S26. DFT simulated atomic structure models of (a) (O_V)NiOOH-CeO_2, (b) CeO_2, (c) NiOOH and (d) NiOOH-CeO_2 for adsorption of urea molecules.

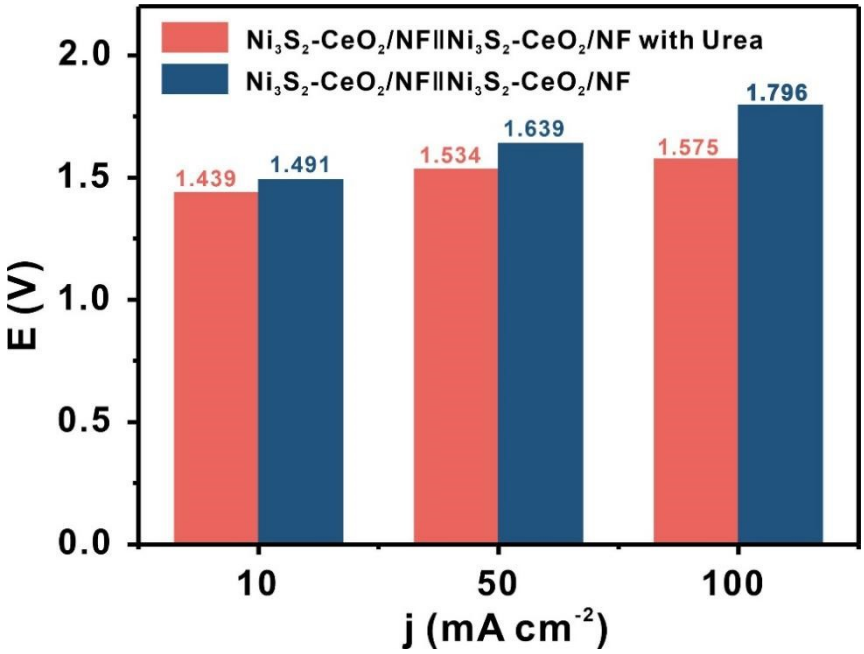

Fig. S27. Cell voltage comparison at current density of 10, 50 and 100 mA cm^{-2} for Ni_3S_2-CeO_2/NF||Ni_3S_2-CeO_2/NF in 1 M KOH/0.50 M urea and 1 M KOH solution.

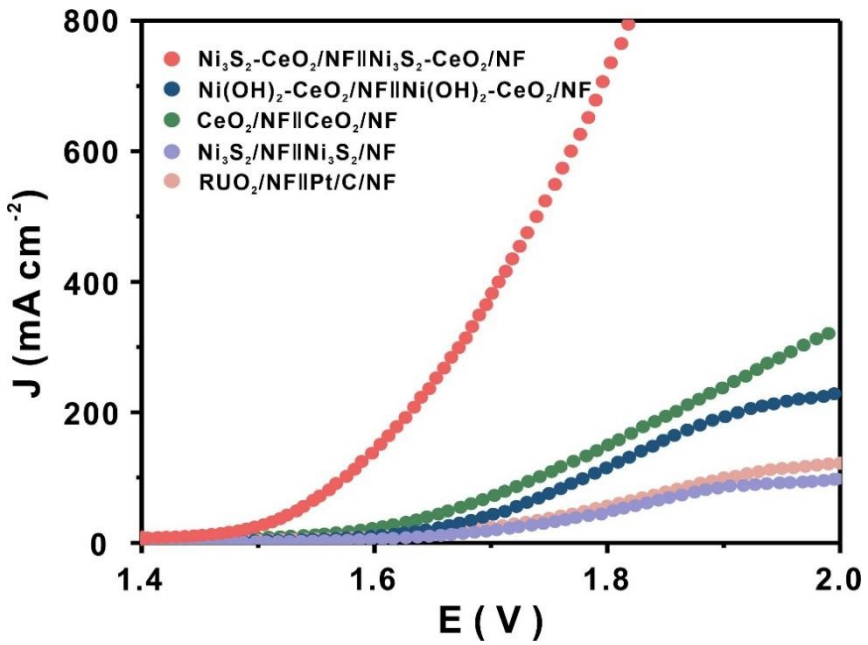

Fig. S28. Polarization curves for urea-assisted overall water electrolysis cell utilizing various catalysts: Ni_3S_2-CeO_2/NF||Ni_3S_2-CeO_2/NF, $Ni(OH)_2$-CeO_2/NF||$Ni(OH)_2$-CeO_2/NF, CeO_2/NF||CeO_2/NF, Ni_3S_2/NF||Ni_3S_2/NF and RuO_2/NF||Pt/C/NF.

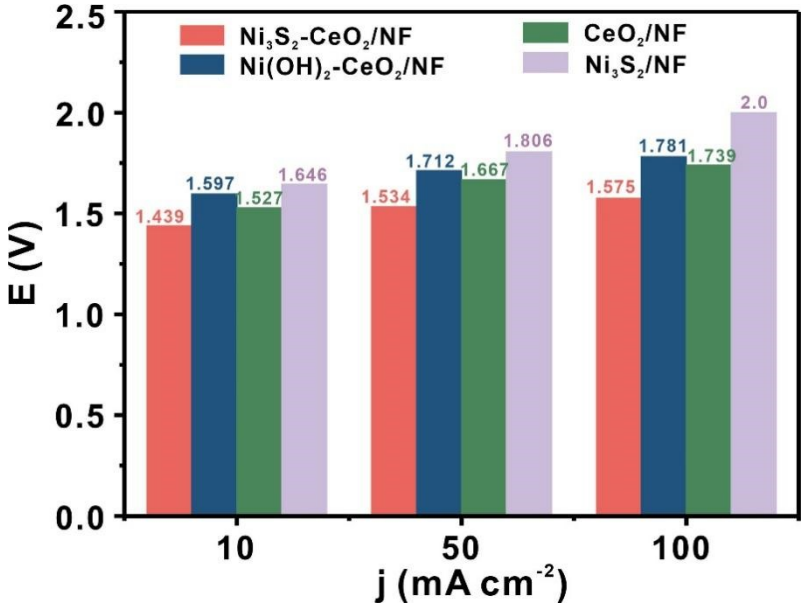

Fig. S29. Cell voltage comparison at current density of 10, 50 and 100 mA cm^{-2} for HER|| UOR system.

Table. S1. Comparison of the UOR performance and Tafel slope of Ni_3S_2-CeO_2/NF with other reported benchmark catalysts.

Catalytic material	Urea Concentration	E@100mA cm^{-2} (V vs RHE)	Tafel slope (mV dec^{-1})	Reference
Ni_3S_2-CeO_2/NF	**0.50 M**	**1.37**	**38.5**	**This Work**
Ni_3S_2–Ni_3P/NF	0.50 M	1.379	16.1	[6]
O-NiMoP/NF	0.50 M	1.41	34	[7]
$NiFe(OH)_x/Ni_3N$ /NF	0.50 M	1.39	26	[8]
a-RuO_2/NiO	0.33 M	1.386	38.4	[9]
Ni_3N/Mo_2N/NF	0.33 M	1.36	34.7	[10]
NiCoP	0.50 M	1.42	59	[11]
MoO_2–NiO/NF	0.50 M	1.402	19.38	[12]
Fe(EDTA)-Ni_3S_2@NF	0.50 M	1.376	29.83	[13]
$NiFeCoSe_2$/NF	0.50 M	1.44	149	[14]
$Mo_{0.2}Ni_{0.8}N/CeO_2$/NF	0.50 M	1.47	53	[15]
Co_2C/MoN/NF	0.50 M	1.42	157	[16]

Table. S2. Comparison of the HER performance of Ni_3S_2-CeO_2/NF with other reported benchmark catalysts.

Catalytic material	Urea Concentration	E@10mAcm^{-2} (mV vs RHE)	Reference
Ni_3S_2-CeO_2/NF	**0.50 M**	**56**	**This Work**
Ni_3S_2–Ni_3P/NF	0.50 M	122	[6]
W-NT@NF-3	0.50 M	88	[17]
$NiSe_2$/$MoSe_2$/CC	0.50 M	79	[18]
Cu-Ni_3S_2/Co_3S_4	0.50 M	79	[19]
MoS_2 NPs/CoS_2 NTs	0.50 M	105.2	[20]
Cu_2S@Ni_3Se_2	0.50 M	106	[21]
NiS/MoS_2@FCP	0.50 M	1.28	[22]
Mn-Ni_2P/NiFe LDH/NF	0.50 M	184	[23]
MnO_2/$MnCo_2O_4$/ NF	0.50 M	200	[24]
Fe_7Se_8@Fe_2O_3/N F	0.50 M	141	[25]

Table. S3. Comparison of the urea-assisted water splitting performance of Ni_3S_2-CeO_2/NF with other reported benchmark catalysts.

Catalytic material	Urea Concentration	E@10mAcm^{-2} (V)	Reference
Ni_3S_2-CeO_2/NF	**0.50 M**	**1.439**	**This Work**
MoO_2–NiO/NF	0.50 M	1.547	[12]
CoS_2-NA/Ti	0.33 M	1.59	[26]
Se-(NiCo)S_x/$(OH)_x$	0.50 M	1.6	[27]
1%Cu-α-$Ni(OH)_2$/NF	0.33 M	1.49	[28]
Cu_2S@Ni_3Se_2	0.50 M	1.48	[21]
Mn-Ni_2P/NiFe LDH/NF	0.50 M	1.494	[23]
MnO_2/$MnCo_2O_4$/NF	0.50 M	1.58	[24]
Fe_7Se_8@Fe_2O_3/NF	0.50 M	1.55	[25]
NiFe/N–C	1.0 M	1.50	[29]
Ni_9S_8/CuS/Cu_2O/NF	0.33 M	1.47	[30]
$NiMoO_4$-MoS_2/NF	0.50 M	1.445	[31]

References

1 G. Kresse and D. Joubert, *Phys. Rev. B*, 1999, **59**, 1758-1775.
2 J. Heyd, G. E. Scuseria and M. Ernzerhof, *J. Chem. Phys.*, 2003, **118**, 8207-8215.
3 J. P. Perdew, K. Burke and M. Ernzerhof, *Phys. Rev. Lett.*, 1996, **77**, 3865-3868.
4 S. Grimme, J. Antony, S. Ehrlich and H. Krieg, *J. Chem. Phys.*, 2010, **132**, 154104.
5 M. Pei, T. Li, G. Chen and K. Ostrikov, *J. Hydrogen Energy.*, 2024, **51**, 975-987.
6. J. Liu, Y. Wang, Y. Liao, C. Wu, Y. Yan, H. Xie and Y. Chen, *ACS Appl. Mater. Interfaces.*, 2021, **13**, 26948-26959.
7 H. Jiang, M. Sun, S. Wu, B. Huang, C.-S. Lee and W. Zhang, *Adv. Funct. Mater.*, 2021, **31**, 2104951.
8 H. Zhang, X. Meng, J. Zhang and Y. Huang, *ACS Sustainable Chem. Eng.*, 2021, **9**, 12584-12590.
9. L. Li, X. Zhang, M. Humayun, X. Xu, Z. Shang, Z. Li, M. F. Yuen, C. Hong, Z. Chen, J. Zeng, M. Bououdina, K. Temst, X. Wang and C. Wang, *ACS Nano*, 2024, **18**, 1214-1225.
10 T. Wang, L. Miao, S. Zheng, H. Qin, X. Cao, L. Yang and L. Jiao, *ACS Catalysis*, 2023, **13**, 4091-4100.
11 X. Ding, L. Pei, Y. Huang, D. Chen and Z. Xie, *Small*, 2022, **18**, 2205547.
12 Z. Deng, X. Du, K. Qian, L. Du, Z. Fang, J. Zhu, J. Hong, F. Wang, T. Li, T. Wei and R. Li, *J. Hydrogen Energy.*, 2024, **62**, 71-80.
13 W. Lv, L. Zhu, X. Kong, H. Shi, C. Wang, R. Zhang and W. Wang, *J. Alloys Compd.*, 2023, **965**, 171292.
14 X. Li, P. Babar, K. Patil, S. Kale, E. Jo, X. Chen, Z. Hussain, J. H. Kim and Y. T. Yoo, *Mater. Chem. Phys.*, 2022, **287**, 126310.
15 L. Meng, L. Zhang, S. Liu, F. Wang and H. Wu, *J. Hydrogen Energy.*, 2023, **48**, 33383-33392.
16 L. Zhang, Y. Wang, J. Cao, R. Zhang, F. Wang and H. Wu, *J. Hydrogen Energy.*, 2022, **47**, 34715-34726.
17 M. Liu, W. Zou, S. Qiu, N. Su, J. Cong and L. Hou, *Adv. Funct. Mater.*, 2024, **34**, 2310155.
18 X. Xu, H. Liao, L. Huang, S. Chen, R. Wang, S. Wu, Y. Wu, Z. Sun and H. Huang, *Appl. Catal. B-Environ.*, 2024, **341**, 123312.
19 H. Su, S. Song, S. Li, Y. Gao, L. Ge, W. Song, T. Ma and J. Liu, *Appl. Catal. B - Environ.*, 2021, **293**, 120225.
20 T. L. Luyen Doan, D. C. Nguyen, K. Kang, A. Ponnusamy, H. I. Eya, N. Y. Dzade, C. S. Kim and C. H. Park, *Appl. Catal. B-Environ.*, 2024, **342**, 123295.
21 L. Lv, Z. Li, H. Wan and C. Wang, *J. Colloid Interface Sci.*, 2021, **592**, 13-21.
22 Y. Zheng, P. Tang, X. Xu and X. Sang, *J. Solid State Chem.*, 2020, **292**, 121644.
23 B. Sang, Y. Liu, X. Wan, S. Xie, G. Zhang, M. Ge, J. Dai, W. Zhang and R.-Q. Li, *Chem. Commun.*, 2023, **59**, 8743-8746.
24 C. Xiao, S. Li, X. Zhang and D. R. MacFarlane, *J. Mater. Chem. A.*, 2017, **5**, 7825-7832.
25 J. Li, X. Du, X. Zhang and Z. Wang, *J. Hydrogen Energy.*, 2022, **47**, 35203-35214.

26 S. Wei, X. Wang, J. Wang, X. Sun, L. Cui, W. Yang, Y. Zheng and J. Liu, *Electrochim. Acta.*, 2017, **246**, 776-782.
27 C. Hu, L. Zhang, Z.-J. Zhao, A. Li, X. Chang and J. Gong, *Adv. Mater.*, 2018, **30**, 1705538.
28 J. Xie, L. Gao, S. Cao, W. Liu, F. Lei, P. Hao, X. Xia and B. Tang, *J. Mater. Chem. A*, 2019, **7**, 13577-13584.
29 J. Zhang, F. Xing, H. Zhang and Y. Huang, *Dalton Trans.*, 2020, **49**, 13962-13969.
30 D. Wei, W. Tang and Y. Wang, *J. Hydrogen Energy.*, 2021, **46**, 20950-20960.
31 J. Zhu, W. Lv, Y. Yang, L. Huang, W. Yu, X. Wang, Q. Han and X. Dong, *New J. Chem.*, 2022, **46**, 10280-10288.